Mechanical characteristics, microstructural evolution, and reinforcement mechanisms for a cement-matrix nanocomposite

Camilla Ronchei [a], Luciana Mantovani [b], Daniela Scorza [a], Andrea Zanichelli [a], Andrea Bernasconi [c], Giacomo Magnani [d], Daniele Pontiroli [d], Michele Sidoli [d], Sabrina Vantadori [a,*]

[a] *Department of Engineering & Architecture, University of Parma, Parco Area delle Scienze 181/A, 43124, Parma, Italy*
[b] *Department of Chemistry, Life Sciences and Environmental Sustainability, University of Parma, Parco Area delle Scienze 157/A, 43124, Parma, Italy*
[c] *Department of Earth Sciences, University of Torino, Via Valperga Caluso 35, 10125, Torino, Italy*
[d] *Department of Mathematical, Physical and Computer Sciences & INSTM, University of Parma, Parco Area delle Scienze 7/A, 43124, Parma, Italy*

ARTICLE INFO

ABSTRACT

The present paper is focused to understand the reinforcement mechanisms exerted by GO nanosheets to both strengthen and toughen cement-matrix composites since, despite intensive research, such mechanisms are still not completely clear. To such an aim, the mechanical characteristics (that is, mechanical strengths and fracture toughness) of a cement-matrix nanocomposite, with the 0.05 % of GO used as an additive, are experimentally investigated at different curing times. Since reinforcement mechanisms are closely related to cement hydration products, they are qualified and quantified by chemical, mineralogical and microstructural analyses performed at the above times of curing. The present investigation leads to the conclusion that the role of both CSH and AFt content is dominant in strengthen and toughen of cement matrix-nanocomposites with GO used as an additive.

1. Introduction

Several research studies have demonstrated the advantages of a new generation of composite materials with nanoscale reinforcement (nanocomposites) such as, for example, graphene nanoplatelets, graphene oxide nanosheets, carbon nanotubes, and silica nanoparticles, due to their superior performances (mechanical, thermal, electrical) compared to conventional microscale reinforcements [1–6].

In such a context, Graphene Oxide (GO) nanosheets have been widely employed as a reinforcing nanomaterial in several cement-matrix composites due to their excellent mechanical performance: Young's modulus of the Tera Pascal magnitude and tensile strength of the order of Mega Pascal. Moreover, GO is highly dispersible in water, avoiding dangerous agglomerations in the cement paste mixture, due to the functional groups attached on the basal planes and edges of GO [7,8]. Such functional groups (hydroxyl, epoxy and carboxyl groups) reduce the Van der Waals forces and increase the electro-static repulsion between GO sheets, facilitating GO dispersion in water. Furthermore, the functional groups prefer to engage in chemical or physical interaction with the cement matrix, thus strengthening its interfacial bonding with

GO sheets [4].

By taking as starting point the above benefits, various Researchers analysed the effects of GO on the mechanical properties of cement-matrix composites. As a matter of fact, several experimental campaigns were performed [9–13], and some of the most interesting results are hereafter presented.

Pan and co-workers performed an exhaustive experimental campaign in order to investigate the mechanical properties of an ordinary Portland cement paste with the addition of 0.05 % (by weight of cement) GO nanosheets [9]. For all the curing times investigated (that is, 7, 14, 28 and 56 days), the Authors found that the addition of GO enhanced both the compressive and the flexural strength with respect to the control specimens. Regarding the elastic modulus, no difference between that of the cementitious composite and the cement paste was observed.

A systematic study on the effects of both the water-binder ratio and the GO sizes on the mechanical performance of a GO-reinforced mortar (0.03 % GO by weight of cement) was carried out by Wang et al. [11]. In comparison to the plain mortar, an increase in terms of compressive, flexural and tensile strengths was observed for specimens with GO at 28

---

* Corresponding author.
E-mail address: sabrina.vantadori@unipr.it (S. Vantadori).

days of curing, especially for the tensile strength with an increase of about 54 %. Moreover, the above mechanical strengths were improved for low values of water-binder ratio or for large sizes of GO (that is >50 μm).

Lee et al. experimentally investigated the compressive strength of a cementitious composite reinforced with GO nanosheets at different replacement ratio [13]. Independently of the above GO replacement ratio, the compressive strength of the cement-matrix composite was higher than that of the plain mixture.

According to the recent literature [11], an unequivocal explanation on the role of the GO in improving the mechanical behaviour of cement-matrix composites is not available. As a matter of fact, the nanoscale mechanisms, by which a small amount of GO is able to be extremely effective in improving the mechanical performance of cementitious composites, are not yet fully understood.

One school of thought examined the GO promoting effect on the cement hydration process. For instance, Lin and co-workers found that the addition of GO in a cement-matrix material accelerated the cement hydration rate [14]. This behaviour was caused by the GO catalytic role; indeed, the functional groups of GO acted as active sites for the interaction with cement hydration products and absorbed water molecules, constituting a water reservoir. Consequently, an acceleration of the hydration reaction was observed, which remarkably influenced the cement-based composite mechanical properties.

Moreover, Lv et al. stated that the GO nanosheets were able to regulate the microstructure of cement hydration crystals [15,16], promoting the formation of flower-like crystals. Such crystals grew in pores of the cement matrix and, forming a strong cross-linking structure, were responsible of tensile/flexural strength improvement of cementitious composites. However, it is worth noting that, according to the discussion reported in Ref. [17], the above flower-like crystals were probably not the cement hydration products but rather calcium carbonate crystals due to carbonation occurred during the specimen preparation for SEM analyses.

In such a context, some Researchers stated that GO had no effects on the cement hydration products, as reported in Refs [9,11,18]. Rather, a chemical interaction between GO and cement matrix was observed by Pan et al. [9]. More precisely, the carboxyl groups of GO reacted with hydration products (in particular with the amorphous phase, CSH, and portlandite crystals, CH) to form strong covalent bonds. Such bonds increased the interfacial load-transfer between GO nanosheets and the cement matrix, thus enhancing the mechanical properties of the cement-matrix composites.

Moreover, the effect of GO on the pore size distribution was investigated in Refs [9,13]. In particular, Lee and co-workers observed that GO-reinforced cementitious composites were characterised by a smaller pore size distribution with respect to plain mixture [13]. As a matter of fact, GO nanosheets filled the micropores within the cement matrix, providing a denser pore structure and, thus, improving the mechanical properties.

Finally, different studies were carried out in order to investigate the effects of GO in controlling the microcracks propagation [9,13,19–21]. For instance, according to Pan et al. [9], the 2D structure of GO nanosheets effectively deflected cracks and/or forced cracks to twist around the nanosheets. Therefore, an increased consumption of energy was required for further crack growth. Moreover, due to the strong interfacial forces between GO functional groups and hydration products, GO nanosheets inhibited the microcrack propagation in the cement-matrix composites [20].

Despite all the above considerations on the GO role in improving the mechanical behaviour of cement-matrix composites, the research in this area is still open and requires further efforts from Scientists. In such a context, the present paper is devoted to the microstructural and mechanical characterisation of a cement-matrix composite reinforced with GO nanosheets at different curing times. In particular, both the chemical, mineralogical and microstructural properties and the mechanical

strengths and fracture toughness are deeply investigated by considering GO-reinforced specimens containing 0.05 % GO nanosheets (by weight of cement). Plain mortar specimens are also considered as control specimens. The difference between the GO-reinforced mortar and the plain one in terms of mechanical and fracture behaviour is discussed in detail by considering the effect of GO on cement hydration products at the different curing times, being such products qualified and quantified by means of the above microstructural characterisation.

The framework of the paper is as follows. Section 2 is dedicated to both the materials employed in the experimental campaign and the specimen preparation. The testing methods for both the microstructural analyses and the mechanical tests are detailed in Section 3, whereas the obtained results are reported in Section 4. Section 5 deals with the discussion of the role of some hydration products in enhancing the mechanical properties of the GO-reinforced mortar. The main conclusions of the present research work are summarised in Section 6. Details on the geometrical sizes and the results related to each tested specimen are listed in Appendix A.

2. Materials and specimens preparation

2.1. Materials

The raw materials of the mortar here examined are commercially available and consist of: limestone Portland cement, silica sand, polycarboxylate superplasticizer (PC) and graphene oxide.

The cement is a 42.5R CEM II/A-LL type (complying with the UNI 9156 and UNI EN 197–1 European standards [22,23]), characterised by Portland Clinker and limestone percentages in the range of 80–94 % and 6–20 %, respectively [24].

The aggregate has silica grain size ranging between 0.08 mm and 2 mm (according to the UNI EN 197–1 European standard [23]).

The additive is a polycarboxylate superplasticizer (PC), provided by BASF Construction Chemicals Italia S.p.a. [25], consisting of an amphipathic surfactant with a 40 % of solid content.

The graphite oxide is obtained from the oxidation of a highly pure graphite powder (average size of 66 μm) carried out by means of the Brodie's method. The Readers interested in the steps of the above procedure can refer to Refs [26,27]. The graphite oxide is characterised by a percentage of carbon and oxygen (by weight) of approximately 75 % and 25 %, respectively.

The 0.05 % of graphite oxide (by weight of cement) is mixed together with 42 % of deionized water (by weight of cement) and 0.3% of PC (by weight of cement) in order to obtain the GO aqueous solution for the preparation of the GO-reinforced specimens. Such a solution is stirred at 60 °C for about 30 min and dispersed at 200 W for about 30 min by using a high intensity ultrasonic processor. At the end of such a procedure, graphene oxide nanosheets are stably dispersed in the aqueous solution.

The microstructural properties of the GO here employed have been already investigated in a previous research work by some of the present authors (for more details see Ref. [28]).

2.2. Specimens preparation

Both reinforced (GO) and plain (PM) specimens are prepared.

The GO specimens are characterised by the following mixture proportions: cement:GO aqueous solution:sand (by weight) equal to 1:0.42:3. More precisely, the dry materials (sand and cement) are put in a concrete mixer; subsequently, the aqueous solution is slowly added to the above cement-matrix mixture and the fresh slurry is mixed for about 2 min. A workability test is performed in accordance to the UNI EN 1015–3 European standard [29] in order to determine the flow. In particular, after jolting the flow table for 15 times in about 15 s, the aqueous solution content in the mixture is enough to produce a flow of about 57.47 %.

The PM specimens, employed as control, are characterised by the

following mixture proportions: cement:water:sand (by weight) equal to 1:0.42:3. Such specimens are prepared by adding a small amount of PC (that is about 0.3 % by weight of cement) to the water, with the aim to guarantee the same workability of the above GO fresh slurry.

It is worth noticing that such mixtures are employed to prepare the specimens for investigating the mechanical characteristics, whereas the sand is not used to prepare the specimens, both reinforced (GO*) and plain (PM*), for microstructural analysis since its presence makes difficult the interpretation of the results in terms of mineralogical analysis. As a matter of fact, the presence of the aggregate, which is typically quartz, entails an overlap of very intense peaks in the diffraction pattern, making the identification of minor phases and amorphous phases particularly complex.

As far as the microstructural analysis is concerned, small cubic moulds (with a side equal to 20 mm) are filled with the fresh slurry, cured in laboratory for 24 h, demoulded and submerged in water for the different times of curing examined, that is, 3, 7, 14, 28, 60, 90 and 120 days.

As far as the mechanical characterisation is concerned, prismatic moulds (with sizes depending on the mechanical properties investigated – see Section 3) are half filled with the fresh slurry and compacted on the flow table with 60 jolts in about 60 s. Then, the moulds are completely filled and jolted on the table for 60 times. Specimens are demoulded after 24 h and submerged in water at room temperature for the different times of curing examined, that is, 3, 7, 28, 90 and 120 days. Note that, for compression testing, the specimens are not casted since the two halves of each broken flexural specimen are directly tested under compression.

For the different curing times being analysed, the number of plain and reinforced specimens employed for both the microstructural analysis (that is, SEM/EDS and X-ray diffraction analysis) and the mechanical characterisation (that is, flexural, compression and fracture testing) is reported in Table 1.

3. Testing methods

The methods for the microstructural and the mechanical characterisation are detailed in the following Sub-Sections.

3.1. Methods for microstructural analysis

The chemical, mineralogical and microstructural properties of the investigated GO-reinforced mortar are experimentally determined through both scanning electron microscopy/energy dispersive spectroscopy (SEM/EDS) and X-ray diffraction (XRD) analyses. In particular, these analyses are carried out on both PM* and GO* specimens. XRD is

also performed on the cement in order to determine its mineralogical composition.

For all the curing times examined, the specimens are dried for about 1 h at a temperature of 30 °C; then, each specimen is divided into two portions: a portion is used for SEM/EDS analysis, whereas the other one is milled for XRD analysis.

3.1.1. SEM/EDS analysis

A fraction of the above PM* and the GO* specimens, with sizes of about $10 \times 10 \times 10$ mm^3, is embedded in epoxy and polished, whereas another fraction is analysed "as it is", in order to observe specific morphologies and shapes of the hydrated crystals.

The analyses are performed by using a SEM/EDS Jeol 6400 Scanning Electron Microscope, equipped with an Oxford EDS (Energy Dispersive System) microprobe. The employed operating conditions are 20 kV and 1.2 mA current, 1 μm beam diameter and 75 s counting time; about 15 analytical points per specimen are taken. SEM images are obtained by using secondary and back-scattered electron detector (BSE), to better assess the microstructure, the presence of composition heterogeneities and to discriminate different phases into the specimens. Moreover, EDS analyses are performed in order to investigate the material chemistry.

3.1.2. X-ray diffraction analysis

The specimens are removed from water, dried in the oven for about 1 h and, then, XRD analysis is immediately performed in order to minimise changing in the mineralogical composition due to the chemical reaction with air. The XRD analyses are carried out by using a Bruker D2 Phaser powder diffractometer (with θ-θ focalizing geometry), which operates at 30 kV and 10 mA with Cu Kα ($\lambda = 1.54178$ Å) radiation. Data are measured in the 5–100° 2θ range, with 0.018° step size and 1 s for step counting time. Each sample is spun at 30 rpm.

In order to identify the major crystalline phases, a qualitative analysis is performed by using the EVA identification software (Bruker EVA, 2018) and the Crystallography Open Database (COD). Note that, only the phases with a concentration higher than 1–2 wt.% can be routinely identified.

Moreover, in order to quantify the major crystalline phases, as well as the amorphous one, the RIR-Rietveld method, with 10 wt.% high purity Si standard, is applied [30]. The Rietveld refinements are performed by the GSAS and EXPGUI packages, and the reference structures used in the refinement are taken from ICSD database [31,32]. Scale factors, cell parameters and pseudo-Voigt profile coefficients for each phase are refined, as well as the instrumental zero. Background is also refined manually, by using a 10 terms Chebychev polynomial. The quantitative results are expressed as the RIR-Rietveld results normalized to 100 wt.%.

3.2. Flexural testing

The flexural strength is experimentally determined by performing three-point bending testing complying with the ASTM C348 standard [33]. The flexural tests are carried out on both the PM and the GO specimens by considering the following curing times: 3, 7, 28, 90 and 120 days (see Table 1).

The experimental setup for the three-point-bending tests is shown in Fig. 1(a). Prismatic beam specimens with nominal sizes equal to 40mm (width, *B*) x 40mm (depth, *W*) x 160mm (length, *L*), and an effective support span of *S*=120mm, are used. The actual sizes of the cross-section of each tested specimen are reported in Appendix A (Tables A.1 and A.2 for the PM and the GO specimens, respectively). Each test is performed, up to failure, under load control (at a rate of 45 Ns^{-1}) by means of the universal testing machine Instron 8862 (load cell up to 100 kN and accuracy of 0.1 %).

The flexural strength, f_{cf}, is computed as a function of the peak load, P_f (experimentally measured during the test), and the geometrical sizes of the specimen, that is [33]:

Table 1
Number of the plain and reinforced specimens employed in both microstructural analysis (named PM* and GO*, respectively) and mechanical characterisation (named PM and GO, respectively) for the different curing times examined.

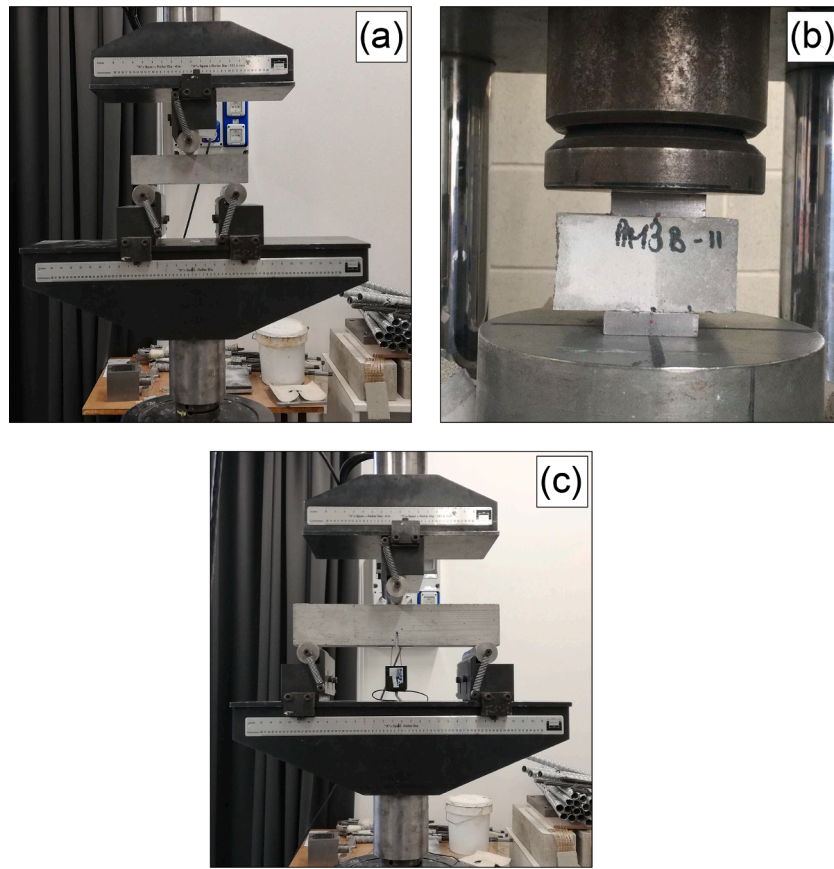| Curing time [days]	Microstructural analysis	Mechanical characterisation		
		Flexural	Compression	Fracture
3	1 PM*	3 PM	6 PM	-
	1 GO*	3 GO	6 GO	-
7	1 PM*	3 PM	6 PM	4 PM
	1 GO*	3 GO	6 GO	4 GO
14	1 PM*	-	-	-
	1 GO*	-	-	-
28	1 PM*	3 PM	6 PM	4 PM
	1 GO*	3 GO	6 GO	4 GO
60	1 PM*	-	-	-
	1 GO*	-	-	-
90	1 PM*	3 PM	6 PM	4 PM
	1 GO*	3 GO	6 GO	4 GO
120	1 PM*	3 PM	6 PM	-
	1 GO*	3 GO	6 GO	-

Fig. 1. Experimental setup for: (a) flexural testing, (b) compression testing and (c) fracture testing.

$$f_{cf} = \frac{1.5 \cdot P_f \cdot S}{B \cdot W^2} \qquad (1)$$

3.3. Compression testing

The compressive strength is experimentally determined by performing compression testing complying with the ASTM C349-18 standard [34]. In particular, compression tests are carried out on both the PM and the GO specimens by considering the following curing times: 3, 7, 28, 90 and 120 days (see Table 1). As mentioned in Section 2.2, the specimens are not casted since the two halves of each broken flexural specimen are directly tested under compression.

The experimental setup for compression tests is shown in Fig. 1 (b). For each specimen, the nominal value of the cross-section area, A_c, is equal to 40×40 mm^2. Each test is performed, up to failure, under load control (at a rate of 2400 ± 200 Ns^{-1}) by means of a standard compression testing machine (load cell up to 300 kN).

The compressive strength, f_c, is computed as a function of the peak load, P_c (experimentally measured during the test), and the geometrical sizes of the specimen, that is [34]:

$$f_c = 0.00062 \cdot P_c \qquad (2)$$

with f_c expressed in MPa.

3.4. Fracture toughness testing

The fracture toughness and the elastic modulus are experimentally determined by performing fracture toughness testing complying with the Rilem draft Recommendation of the TC89-FTM Technical Committee [35], also summarised in Ref. [36], and the Modified Two-Parameter Model (MTPM) [37–39]. The fracture toughness tests are carried out on

both the PM and the GO specimens by considering the following curing times: 7, 28, and 90 days (see Table 1).

The experimental setup for three-point-bending tests is shown in Fig. 1(c). Notched prismatic beam specimens of nominal sizes equal to 30mm (width, B) x 60mm (depth, W) x 300mm (length, L), with an effective support span S=240mm, are used. The notch, realised in the lower part of the middle cross-section by using a circular saw, has a nominal length (a_0) equal to 20mm and a nominal width equal to 1.45mm. The actual sizes of the specimen cross-section and notch length for each tested specimen are reported in Appendix A (Tables A.5 and A.6 for the PM and the GO specimens, respectively). Each test is performed under Crack Mouth Opening Displacement (CMOD) control (at a rate of 0.15 mmh^{-1}) by means of the universal testing machine Instron 8862 equipped with a clip gauge (travel up to 4 mm and accuracy of ± 0.05 %). During each fracture toughness test, it is required to perform: (i) a complete unloading of the specimen (under load-controlled mode) once about 95 % of the peak load, P_{max}, is reached in the post-peak stage and (ii) a reloading of the specimen (under CMOD-controlled mode) up to its failure. At the end of each test, the angle between the crack path and the loading direction (named in the following kinking angle), α, is measured according to the MTPM in order to take into account possible crack deflection due to the inhomogeneities embedded in the cementitious matrix. More precisely, when the kinking angle is not constant along the crack path, it is assumed that the crack at P_{max} is characterised by two branches. Therefore, the following procedure is used to compute α: (i) if the length of the first crack branch is less than the second one, the angle is assumed to be equal to the orientation of the second branch; (ii) whereas, if the length of the second crack branch is less than the first one, the angle is assumed to be equal to the orientation of the first branch. Moreover, when the fracture surface is not plane, the mean value of α is computed by averaging the values related to front- and back-side of the specimen. The mean values of the kinking angle are

listed in Tables A.5 and A.6 for the PM and GO specimens, respectively.

The fracture toughness, $K_{(I+II)C}^S$ (that is, the mixed mode critical Stress-Intensity Factor), and the elastic modulus, E, are computed as a function of P_{max}, α, the initial, C_i, and unloading, C_u, linear elastic compliances (experimentally measured during each test) and the geometrical sizes of the specimen, as prescribed by the MTPM. For an exhaustive overview of all the peculiarities of such a model, the reader can refer to the original paper [37].

4. Results

The chemical, mineralogical and microstructural results of both the PM* and the GO* specimens are determined according to the test methods reported in Section 3.1. The mechanical properties in terms of flexural and compressive strengths are obtained through the test methods presented in Sections 3.2 and 3.3, respectively; the test method described in Section 3.4 is employed for the computation of both the fracture toughness and the elastic modulus. All the above results are discussed in detail in the following sections.

4.1. Microstructural analysis results

By considering the SEM/EDS analyses for all the curing times examined, no differences in terms of crystalline morphologies are observed between the PM* and the GO* specimens.

More precisely, the SEM/BSE images of the PM* and the GO* specimens at 14 days of curing, reported in Fig. 2(a) and (b) respectively, do not show significant differences in morphology. More precisely, the specimens are composed of calcium silicate hydrate, CSH (that is, the amorphous phase of the cement hydration products), crystals of tricalcium silicate, C_3S, and dicalcium silicate, C_2S, with crystal sizes ranging between 30 and 50 μm. Moreover, crystals of calcium hydroxide, CH

(portlandite), with a size range of 40–80 μm, can be observed.

By comparing the PM* and the GO* specimens at a curing time of 28 days, no differences are observed (see Fig. 2(c) and (d)). In particular, a lower content of C_3S and C_2S small crystals (those with higher exposed surface area and reactivity) and a higher content of both large CH crystals and CSH phase are observed with respect to the specimens at 14 days of curing, independently of the specimen type.

Since the morphology at a given curing time does not change regardless of the specimen type, let us consider the SEM/BSE images of the GO* specimens at different curing times, as reported in Fig. 3. In particular, at 7 days of curing (see Fig. 3(a)), C_3S and C_2S crystals exhibit the typical re-absorption morphology, suggesting that the cement hydration reaction has not yet finished.

The cement hydration products can be easily identified at 28 days of curing as reported in Fig. 3(b) in terms of portlandite (CH), with the characteristic hexagonal shape crystals, and in Fig. 3(c) in terms of ettringite (AFt), characterised by needle-like crystals.

In specimens characterised by 60 days of curing, C_3S and C_2S crystals appear almost completely reacted, showing only remnants of the initial crystals (Fig. 3(d)).

By considering the longer curing times examined (that is, 60, 90 and 120 days), the observed mineralogical phases are the same as those shown in Fig. 3(b) and (c), both in terms of size and shape.

For all curing times examined, rhombohedral crystals are observed on the exposed surface of calcite (Fig. 3(e)); due to their shape and location, it can be assumed that these crystals are formed during the carbonation occurred between the specimen preparation and the SEM/EDS analysis.

XRD patterns confirm the phases observed by the above SEM analysis, further providing an accurate quantification of such phases by means of the Rietveld method.

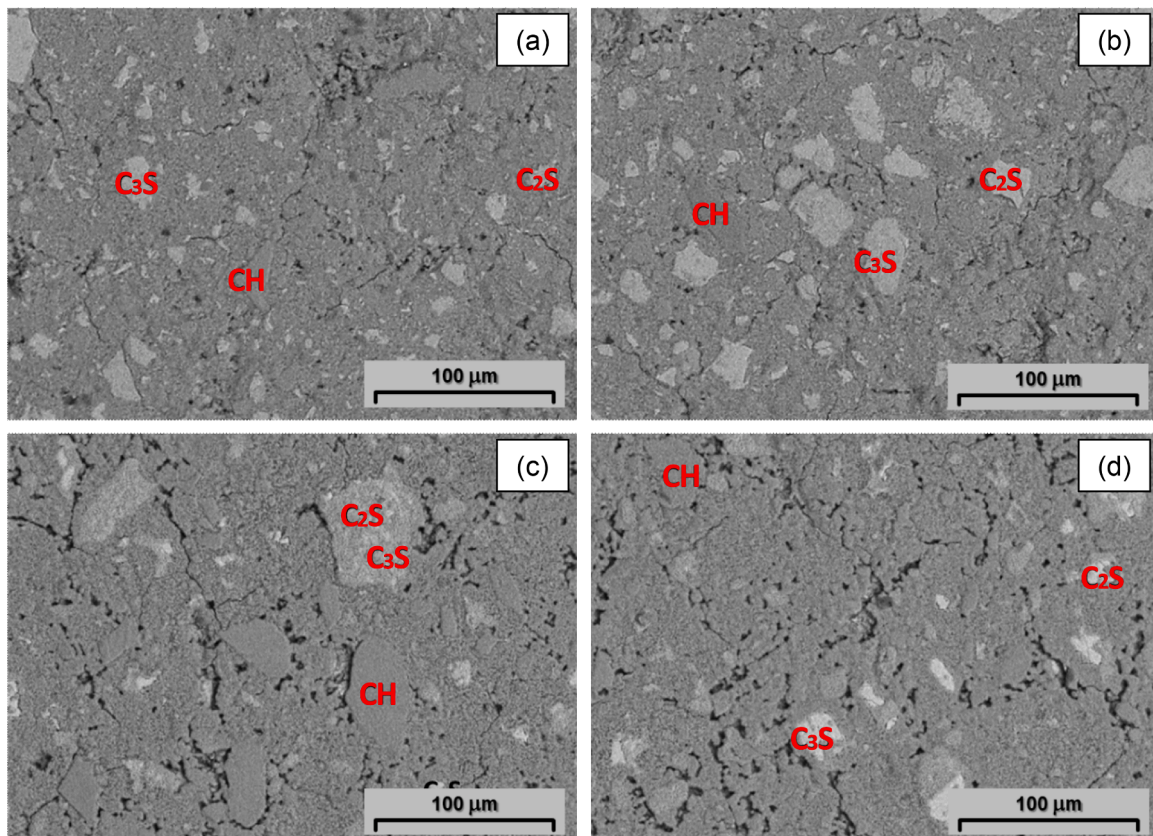As far as the cement is concerned, its XRD pattern is shown in Fig. 4,

Fig. 2. SEM/BSE images of the: (a) PM* and (b) GO* specimens at 14 days of curing and the (c) PM* and (d) GO* specimens at 28 days of curing.

Fig. 3. SEM/BSE images of the GO* specimens at different curing times: (a) 7 days, (b) and (c) 28 days and (d) 60 days. The rhombohedral crystals observed on the exposed surface of calcite are shown in Figure (e).

Fig. 4. XRD pattern of the cement.

where the following mineralogical phases are identified (in abundance order): tricalcium silicate C_3S (Ca_3SiO_5), calcite ($CaCO_3$), dicalcium silicate C_2S (Ca_2SiO_4), tetracalcium aluminoferrite C_4AF ($FeCa_2AlO_5$), tricalcium aluminate C_3A ($Ca_3Al_2O_6$) and gypsum ($Ca_2SO_4 \cdot 2H_2O$).

As far as the cement-matrix specimens are concerned, the same results in terms of XRD pattern are observed, independently of both the specimen type and the curing time. By considering, for example, the cement-matrix specimens at 28 days of curing, no substantial differences are observed between the PM* and the GO* specimens, since the same hydration products can be identified in both specimens, that is: portlandite, CH, ettringite, AFt, and to a lesser extent monosulfate, AFm (see Fig. 5). Moreover, C_3S, C_2S and calcite are still present in both the XRD patterns.

The quantification of the XRD phases, performed by means of the Rietveld method, is reported in Table 2 for both the PM* and the GO* specimens at the different curing times examined.

According to Table 2, the main hydration product is the amorphous phase, CSH, which represents more than 50 wt% in both the PM* and the GO* specimens for all curing times examined. Amongst the crystalline phases, portlandite, CH, and ettringite, AFt, are present in both the PM*

Fig. 5. XRD patterns of both the PM* and the GO* specimens at 28 days of curing (*: internal standard).

Table 2

Quantitative results (wt%) by means of the Rietveld refinement method for both the PM* and the GO* specimens at the different curing times examined ([a]emicarbonate and hydrotalcite).

Curing time [days]	C_3S		C_2S		C_4AF		AFt		AFm[a]		CH		$CaCO_3$		CSH	
	PM*	GO*	PM*	GO*	PM*	GO*	PM*	GO*	PM*	GO*	PM*	GO*	PM*	GO*	PM*	GO*
3	5.4	3.8	4.9	3.9	2.6	2.3	7.9	6.5	–	–	6.5	5.6	17	9.9	55.7	68.0
7	4.3	3.1	8.1	4.9	2.5	1.2	7.4	7.1	0.7	1.3	7.5	8.8	11.1	8.9	58.4	64.5
14	2.1	1.9	4.2	4.5	1.9	0.7	7.3	6.8	1.8	1.9	8	9.5	13.4	9.5	61.3	65.2
28	0.8	1.7	3.3	3.4	0.8	0.6	8.5	6.3	2.1	1.6	7.5	6.7	13.6	9.6	63.4	70.1
60	0.7	0.4	2.6	2.3	0.5	0.3	7.9	6.7	2.1	2.6	7.8	7.8	15.1	9.1	63.3	71.1
90	1.6	0.2	2.4	1.7	0.9	0.3	8.2	5.4	2.3	1.6	9.8	7.4	12	14.5	62.8	68.9
120	0.6	0.2	0.9	0.3	0.3	0.2	8.5	5.8	2.9	1.9	7.9	9.1	18.2	10.3	60.7	72.2

and the GO* specimens with a percent by weight ranging between 5–10 % by varying the curing time. Also the monosulfate, AFm, is identified in both specimen types, but in a smaller percent by weight with respect to the other crystalline phases (that is, CH and AFt). The mineralogical phases of the cement, that is, C_3S, C_2S and C_4AF, are still present, regardless of the specimen type. However, these phases show a significant decrease after 28 days of curing, stabilising at almost constant values. It is important to point out that C_3A and gypsum are not observed since they are the first minerals to react during the cement hydration [40].

In order to better compare the quantities of the different phases present in the PM* and the GO* specimens, the percent by weight of such phases is plotted in Fig. 6 as a function of the curing time.

In particular, the amorphous phase is the main constituent, varying between 55 and 73 wt% (Fig. 6(a)). It increases by increasing the curing time for both specimen types, but such an increase is greater for the GO* specimens (increase of about +12 % from 7 to 120 days of curing). In the

case of the PM* specimens, the CSH increase is clearly visible up to 14 days, whereas from 14 to 120 days of curing it remains stable.

Amongst the crystalline phases, the content of ettringite, AFt, ranges from approximately 7 % to 9 % by weight, without significant variations during the curing time, for the PM* specimens (Fig. 6(b)); a lower content and a slight decrease of such phases, by increasing the curing time, is observed for the GO* specimens compared to the PM* ones.

The percent by weight of the portlandite crystals, CH, varies from 5 % to 10 % for both the PM* and the GO* specimens (Fig. 6(c)). The CH percent by weight in the GO* specimens increases up to 14 days of curing (where the maximum value is reached) and then decreases at 28 days, increasing again at 120 days. In the PM* specimens, the percent by weight of CH is approximately constant up to 60 days of curing, and then reaches the maximum value at 90 days (approximately equal to the maximum of the GO* specimens).

The last hydration crystals, that is the monosulfonate, AFm, is present in a very low percentage in both the PM* and the GO* specimens
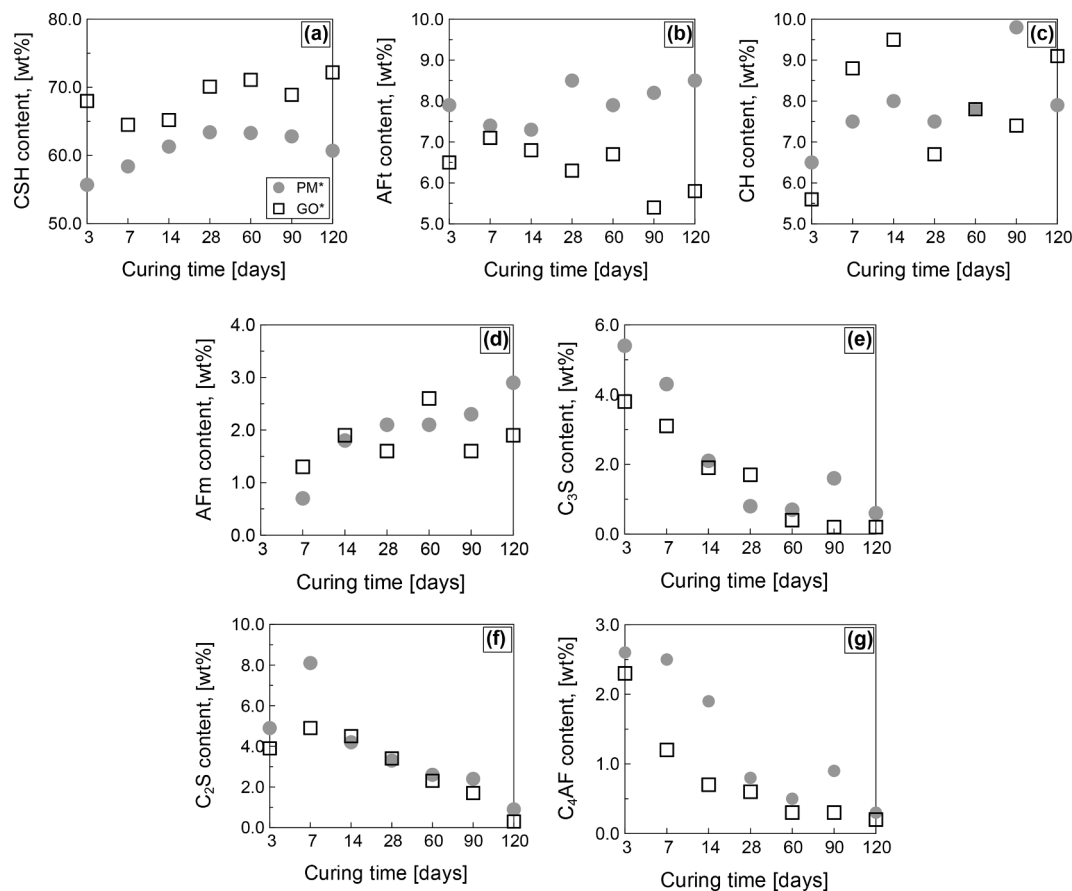

Fig. 6. Percent by weight of the hydration products in the PM* and the GO* specimens against the curing time: (a) amorphous CSH, (b) ettringite AFt, (c) portlandite CH, (d) monosulfonate AFm, (e) tricalcium silicate C_3S, (f) dicalcium silicate C_2S and (g) tetracalcium aluminoferrite C_4AF.

(Fig. 6(d)). Note that, such a crystalline phase is not present in the specimens after 3 days of curing, beginning to form from 7 days. In the PM* specimens, the percent by weight of AFm increases by increasing the curing time; in the GO* specimens, the content of such a phase is approximately constant, with the exception of the 60 days of curing where AFm percent by weight attains its maximum value.

Finally, the percent by weight of the main cementitious phases, that is C_3S, C_2S, and C_4AF, is reported in Fig. 6(e)–(g), respectively, as a function of the curing time. Such phases show a significant decrease during the first 28 days of curing and, then, stabilise at constant values for both the PM* and the GO* specimens.

It can be concluded that, from a mineralogical and microstructural point of view, the addition of GO mainly results in the variation of two hydration products content, that is: the increase of the amorphous phase and the decrease of the ettringite with respect to the plain specimens.

4.2. Flexural strength

The experimental values of the peak load, P_f, and the computed values of the flexural strength, f_{cf}, related to all tested specimens are reported in Appendix A (see Tables A.1 and A.2). For each specimen type (that is, PM or GO specimens) and curing time, the mean value and the standard deviation of f_{cf} are listed in Table 3.

As can be noticed according to Table 3, for both the PM and the GO specimens, the mean value of f_{cf} increases up to 90 days of curing (with the same growth rate for the two types of specimens), and then an almost constant value is achieved between 90 and 120 days. Regarding the standard deviation, its value increases as the curing time increases (except for 28 days of curing) for the GO specimens, whereas for the PM ones the most dispersed results occur at 28 days of curing.

The flexural strength mean value of the GO specimens is always greater than that of the PM specimens, for all the curing times being considered. The relative difference (in percentage) between f_{cf} (in terms of mean value) for the GO specimens and that for the PM ones is also reported in Table 3 for each curing time examined. In particular, such a difference is always positive and almost constant between 3 and 7 days of curing, reaching its maximum value at 28 days (equal to +10.54 %); at 90 and 120 days of curing the relative increment is quite constant and approximately equal to +7.00 %.

4.3. Compressive strength

The computed values of the compressive strength, f_c, related to all tested specimens are reported in Appendix A (see Tables A.3 and A.4). For each specimen type (that is, PM or GO specimens) and curing time,

the mean value and the standard deviation of f_c are listed in Table 4.

As can be noticed according to Table 4, for both the PM and the GO specimens, the mean value of f_c increases up to 28 days of curing, and then an almost constant value is achieved between 28 and 120 days. Regarding the PM specimens, the maximum value of the standard deviation is achieved at 3 days of curing, whereas the results for the GO specimens are generally less dispersed than those of the PM ones.

With the exception of 3 days of curing, the compressive strength mean value of the GO specimens is completely comparable to that of the PM ones, independently of the curing times. As a matter of fact, the relative difference (in percentage) between f_c (in terms of mean value) for the GO specimens and that for the PM ones, reported in Table 4, is lower than about ±3.00 %.

4.4. Fracture toughness and elastic modulus

The results related to fracture tests in terms of load against CMOD curves are reported in Fig. 7 for the PM and the GO specimen types by considering the different curing times examined. In particular, the experimental scatters of the load-CMOD curves, obtained by retracing their external contour, are reported in the above figure in grey.

By examining the above curves, it can be observed that, for each curing time examined, both the initial slope and the trend of the softening branch are similar for the PM and the GO specimens. The value of the peak load, P_{max}, is greater for the GO specimens than for the PM specimens for each curing time being considered, even if the CMOD value in correspondence of P_{max} is quite constant. Moreover, from such graphs it can be seen that the scatter of the experimental curves is generally narrower for the GO specimens compared to that of the PM ones, and this is particularly evident at 7 and 28 days of curing.

The experimental values of P_{max}, kinking angle, α, and the computed values of both the fracture toughness, $K^S_{(I+II)C}$, and the elastic modulus, E, related to all tested specimens are reported in Appendix A (see Tables A.5 and A.6). For each specimen type and curing time, the mean value and the standard deviation of both $K^S_{(I+II)C}$ and E are listed in Table 5.

As can be noticed according to Table 5, for both the PM and the GO specimens, the mean value of $K^S_{(I+II)C}$ increases up to 90 days of curing. The standard deviation values are generally small and almost independent of the curing time, for both the specimen types.

The fracture toughness mean value of the GO specimens is always greater than that of the PM specimens, for all the curing times being considered. The relative difference (in percentage) between $K^S_{(I+II)C}$ (in terms of mean value) for the GO specimens and that for the PM ones is

Table 3
Mean value and standard deviation of the flexural strength, f_{cf}, for each specimen type and curing time being analysed. The relative difference between the f_{cf} mean value for the GO specimens with respect to that for the PM specimens is also reported.

Specimen type	Flexural strength, f_{cf} [MPa]				
	3 days	7 days	28 days	90 days	120 days
PM	4.59 ± 0.08	6.52 ± 0.27	8.92 ± 1.07	10.60 ± 0.60	10.58 ± 0.30
GO	5.04 ± 0.44	7.11 ± 0.59	9.86 ± 0.36	11.35 ± 0.83	11.32 ± 1.17
Relative difference	*+9.90 %*	*+9.09 %*	*+10.54 %*	*+7.08 %*	*+7.04 %*

Table 4
Mean value and standard deviation of the compressive strength, f_c, for each specimen type and curing time being analysed. The relative difference between the f_c mean value for the GO specimens with respect to that for the PM specimens is also reported.

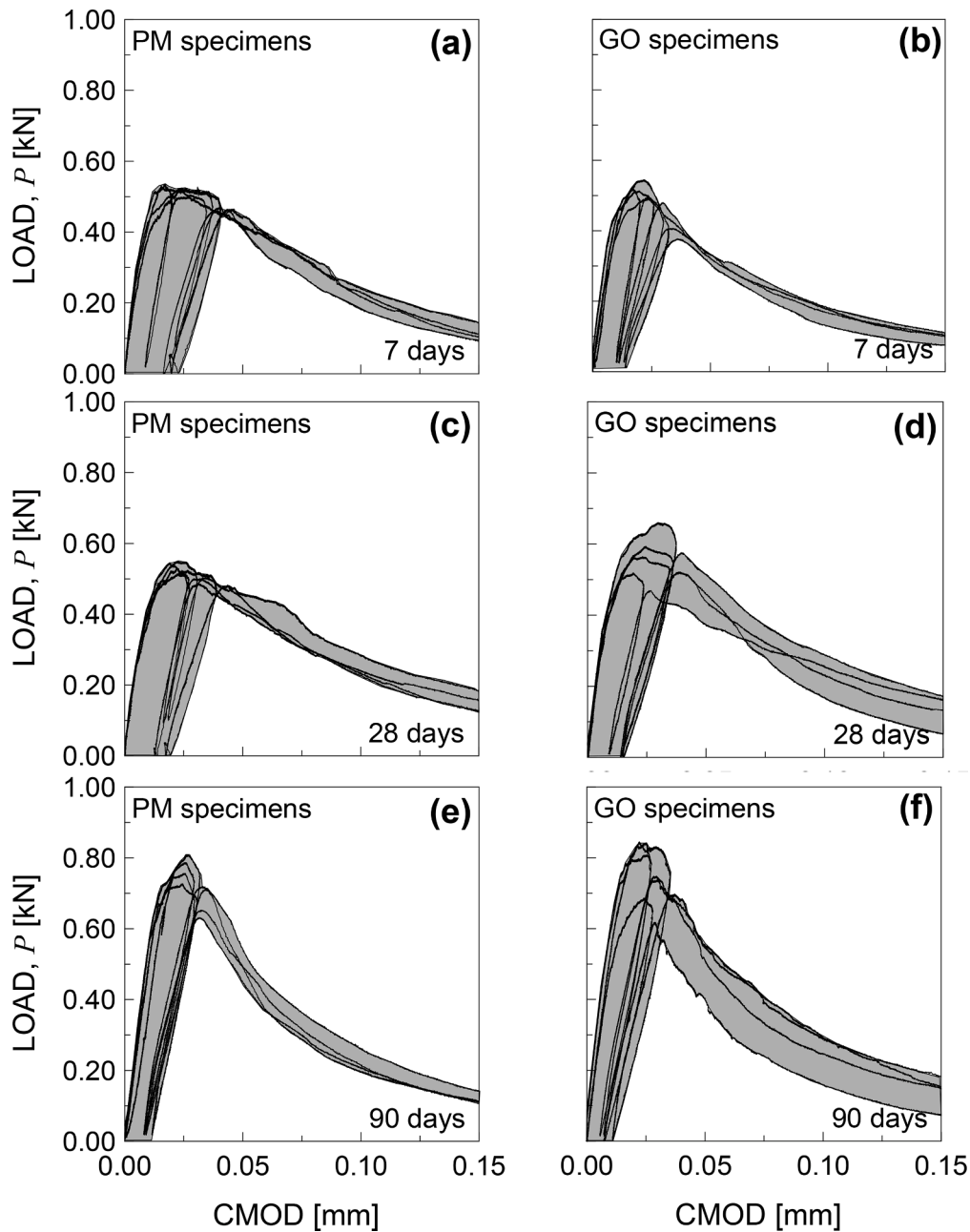| Specimen type	Compressive strength, f_c [MPa]				
	3 days	7 days	28 days	90 days	120 days
PM	29.52 ± 8.76	49.95 ± 7.07	55.74 ± 6.06	56.05 ± 3.11	57.47 ± 3.36
GO	36.38 ± 1.76	48.43 ± 5.62	57.21 ± 2.51	55.66 ± 4.06	58.85 ± 7.53
Relative difference	*+23.24 %*	*-3.05 %*	*+2.64 %*	*-0.70 %*	*+2.39 %*

Fig. 7. Load-CMOD curves for the: (a) PM and (b) GO specimens at 7 days of curing, the (c) PM and (d) GO specimens at 28 days of curing and the (e) PM and (f) GO specimens at 90 days of curing. The experimental scatters of the load-CMOD curves are reported in grey.

Table 5
Mean value and standard deviation of the fracture toughness, $K^S_{(I+II)C}$, and the elastic modulus, E, for each specimen type and curing time being analysed. For both $K^S_{(I+II)C}$ and E, the relative difference between the mean value for the GO specimens with respect to that for the PM specimens is also reported.

Specimen type	Fracture toughness, $K^S_{(I+II)C}$ [MPa·m$^{0.5}$]			Elastic modulus, E [GPa]		
	7 days	28 days	90 days	7 days	28 days	90 days
PM	0.52 ± 0.04	0.56 ± 0.05	0.78 ± 0.02	22.83 ± 1.90	23.21 ± 1.20	22.78 ± 0.92
GO	0.56 ± 0.05	0.65 ± 0.03	0.86 ± 0.03	21.20 ± 0.88	23.82 ± 1.37	25.10 ± 0.93
Relative difference	*+8.08 %*	*+15.59 %*	*+10.00 %*	*-7.14 %*	*+2.63 %*	*+10.18 %*

also reported in Table 5. In particular, such a difference is always positive and equal to about +8.00 % at 7 days of curing, reaching its maximum value at 28 days (being equal to +15.59 %); at 90 days of curing the relative increment has a slight decrease, reaching a value of +10.00 %. The above trend is completely similar to that observed for the flexural strength and, therefore, it can be supposed that an almost constant value is achieved also for the fracture toughness after 90 days of curing.
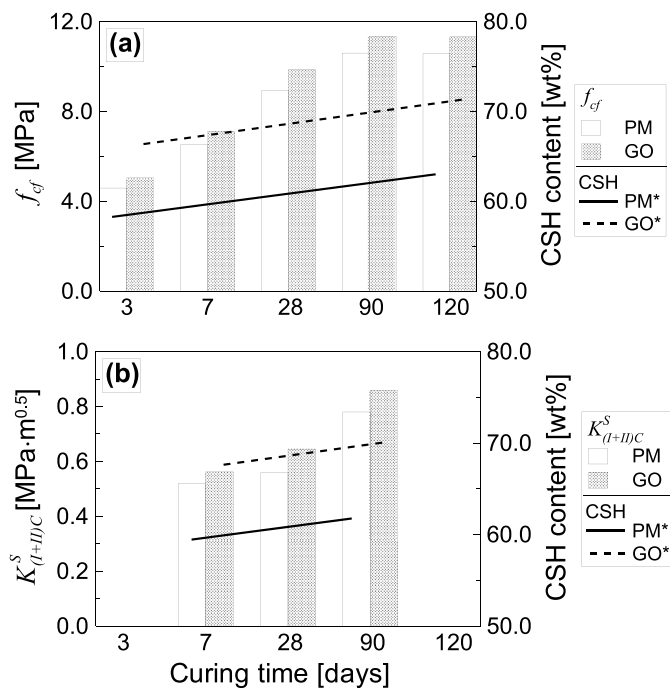
Fig. 8. Results obtained in terms of (a) flexural strength and (b) fracture toughness for the PM (empty bars) and the GO (dotted bars) specimens. The linear interpolation of the CSH content measured for the PM* (solid lines) and the GO* (dashed lines) specimens is also reported.

From Table 5, it can be observed that, for the PM specimens, the mean value of E is almost constant as the curing time increases, whereas, for the GO specimens, it increases with the curing time, especially between 7 and 28 days. The standard deviation values of both the PM and the GO specimens are completely comparable and included in the range between 0.8 and 1.9 GPa.

At 90 days of curing, the increment (in percentage) between E (in terms of mean value) for the GO specimens and that for the PM ones, reported in Table 5, is maximum and equal to about 10 %.

5. Discussion

As previously introduced in Section 4, the addition of GO nanosheets to the examined plain mortar mainly results in:

(a) a quantitative variation of two hydration products (i.e. an increase in amorphous phase, CSH, and a decrease in ettringite, AFt) compared to those present in the PM* specimens, for each curing time considered;
(b) an increase in mechanical properties, and in particular in the flexural strength and fracture toughness, with respect to those related to plain mortar, for each curing time.

The role of each of the above hydration products on the mechanical properties of the GO-reinforced mortar is discussed in the following Sub-Sections.

5.1. The role of the amorphous phase on the mechanical properties

It is well known that CSH (that is, the amorphous phase) is the primary reaction product of cement hydration (constituting over 60 % by volume of hydrated cement) and is responsible for the durability and strength of cement-matrix materials [41].

In Fig. 8, the results in terms of flexural strength (Fig. 8(a)) and fracture toughness (Fig. 8(b)) are combined with those in terms of CSH content. More precisely, for each curing time examined, the mean values

of both the flexural strength and fracture toughness computed for the PM specimens are represented by empty bars, whereas those for the GO specimens by dotted bars. Moreover, a linear interpolation of the CSH content measured for the PM* specimens is represented by a solid line, whereas that measured for the GO* specimens by a dashed line.

It can be observed that by increasing the CSH content (that is by increasing the curing time) the above mechanical properties increase and that, for a given curing time, to a higher CSH content (observed for the GO-reinforced specimens) corresponds a greater value of the above mechanical properties.

The present results agree with some recent findings available in the literature [7]. More precisely, Qureshi and Panesar performed an experimental campaign on cement composites reinforced with GO (at different concentrations), finding that the presence of GO increased the formation of the amorphous phase compared to the control specimens. Moreover, they observed that the flexural strength of the GO specimens was improved with respect to that of the control ones, with the optimum performance in correspondence of 0.04 % GO concentration.

The abovementioned beneficial role of the amorphous phase on the mechanical properties could be explained by examining first of all the interaction (of chemical nature) between the cement matrix and GO. As already discussed in the Introduction, the carboxylic functional groups of GO react with cement hydration products, and in particular with CSH, thus forming robust covalent bonds between the surface of GO and the cement matrix, which enhance the interfacial load-transfer mechanisms from the cement matrix to GO.

In such a context, it can be stated that the observed increase of CSH in the GO specimens promotes an excellent interfacial bonding with the cement matrix, resulting in improved flexural strength and fracture toughness with respect to the PM specimens.

As far as the compressive strength is concerned, it is worth noting that it is not affected by the interfacial load-transfer mechanisms and, indeed, the compressive strength mean value of the GO specimens is completely comparable to that of the PM ones (with a maximum variation in absolute value lower than 3 % starting from 7 days of curing).

Another explanation regarding the role of the amorphous phase in improving the mechanical properties of the GO specimens can be found in the observation that the addition of GO conducts to the formation of hydration products within the cement pores [8]. In particular, micropores smaller than ≈ 10 μm are commonly filled with CSH, and, consequently, the GO addition in cement-matrix materials allows the reduction of the greater sized pores.

However, the above role of GO in filling micropores is not confirmed by the present experimental results. As a matter of fact, pores are not detected in SEM/BSE images related to both the PM* and the GO* specimens. This aspect is due to the fact that specimens employed for the SEM/EDS analysis are free of sand (see Section 2), whereas sand is added to the mixture of specimens casted for the mechanical tests. In this latter case, the addition of sand increases the air incorporated during the mixing, thus facilitating the formation of pores.

Consequently, it is only possible to assume that the reinforced specimens are characterised by a pore distribution more shifted towards smaller sizes with respect to the PM specimens, thereby improving the mechanical properties of the nanomodified mortar.

5.2. The role of the ettringite on the mechanical properties

Another relevant reaction product of cement hydration (constituting over 5 % by volume of hydrated cement) is the ettringite, Aft (forming due to the chemical reaction between C_3A, gypsum and water) and it is well known that is responsible for material cracking [42].

In Fig. 9, the results in terms of flexural strength (Fig. 9(a)) and fracture toughness (Fig. 9(b)) are combined with those in terms of AFt content. More precisely, for each curing time examined, the mean values of both the flexural strength and fracture toughness computed for the PM specimens are represented by empty bars, whereas those for the GO

specimens by dotted bars. Moreover, a linear interpolation of the AFt content measured for the PM* specimens is represented by a solid line, whereas that measured for the GO* specimens by a dashed line.

It can be observed that, for the GO specimens the above mechanical properties are greater with respect to those for the PM specimens for each curing time examined and that, for a given curing time, the AFt content is lower for the GO specimens with respect to that for the PM specimens.

The beneficial role of a low AFt content on the mechanical properties could be explained by considering the growing mechanism of such crystals that, growing fast, exert an expansive force within the matrix, leading to cracking. Therefore, in the GO specimens, characterised by a lower AFt content with respect to the PM ones, the matrix is less damaged by the above mechanism, leading to better mechanical and fracture performances. Note that, to the best knowledge of the present authors, this aspect is not investigated in any literature work.

6. Conclusions

In the present paper, the microstructural and mechanical characterisation of a cement-matrix composite reinforced with GO nanosheets at different curing times have been experimentally investigated. In particular, both the chemical, mineralogical and microstructural properties and the mechanical strengths and fracture toughness have been deeply investigated by considering GO-reinforced specimens containing 0.05 % GO nanosheets (by weight of cement). Plain mortar specimens have been also considered as control specimens. The difference between the GO-reinforced mortar and the plain one in terms of mechanical and fracture behaviour has been discussed in detail by considering the effect of GO on cement hydration products at the different curing times, being such products qualified and quantified by means of the above microstructural characterisation.

Regarding the microstructural results from the SEM/EDS analyses, no differences in terms of crystalline morphologies have been observed

between the PM* and the GO* specimens for all the curing times examined. In particular, starting from 28 days of curing, the cement hydration products have been easily identified, that is portlandite (hexagonal shape crystals) and ettringite (needle-like crystals). XRD patterns have confirmed the phases observed by SEM analyses, in addition to provide a precise quantification through the Rietveld method. In particular, the addition of GO mainly results in the variation of two hydration products content, that is, for each curing time, the increase of CSH content and the decrease of the AFt content with respect to the PM* specimens.

As far as the mechanical characterisation is concerned, the mean values of both the flexural strength and fracture toughness of the GO specimens are always greater than those of the PM specimens, for all the curing times being considered. On the other hand, the compressive strength and elastic modulus mean values of the GO specimens are quite similar to those of the PM ones.

Finally, the role of CSH and AFt on the mechanical properties of the examined reinforced mortar has been discussed, reaching the following conclusions:

- the increase of CSH content in the reinforced specimens has promoted an excellent interfacial bonding with the cement matrix (strong covalent bonds between the carboxyl groups of GO and CSH), resulting in improved flexural strength and fracture toughness with respect to the plain mortar;
- the highest CSH content observed in the reinforced specimens has suggested that such specimens are characterised by a greater amount of small pores with respect to the PM specimens, thereby improving the mechanical properties of the GO reinforced mortar;
- the decrease of AFt in the reinforced specimens with respect to the PM ones has led to better mechanical properties for the former type of specimens, even if the role of GO in reducing AFt content is not yet understood.

CRediT authorship contribution statement

Camilla Ronchei: Writing – original draft, Investigation, Formal analysis. **Luciana Mantovani:** Writing – original draft, Investigation, Formal analysis. **Daniela Scorza:** Writing – review & editing, Validation, Investigation. **Andrea Zanichelli:** Writing – review & editing, Validation, Investigation. **Andrea Bernasconi:** Writing – review & editing, Formal analysis. **Giacomo Magnani:** Writing – review & editing, Resources. **Daniele Pontiroli:** Writing – review & editing, Resources. **Michele Sidoli:** Writing – review & editing, Resources. **Sabrina Vantadori:** Writing – review & editing, Supervision, Methodology, Funding acquisition, Conceptualization.

Declaration of competing interest

The authors declare that they have no known competing financial interests or personal relationships that could have appeared to influence the work reported in this paper.

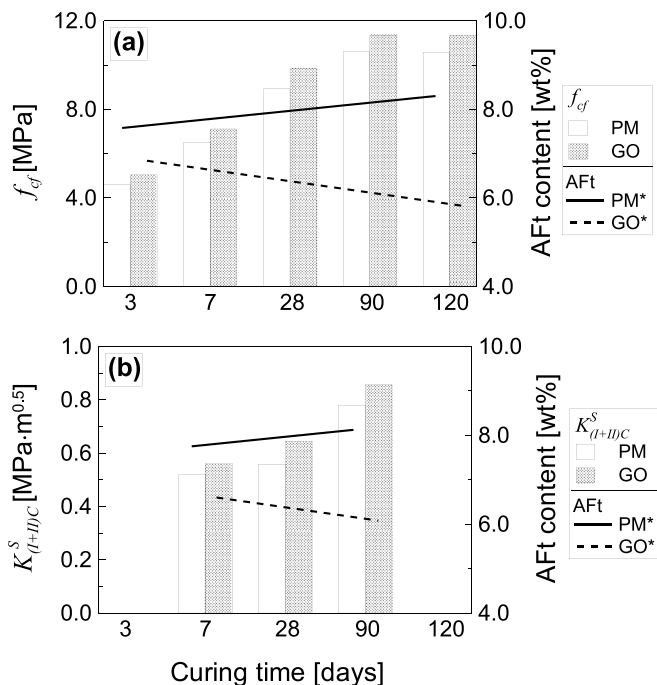**Data availability**

Data will be made available on request.

Fig. 9. Results obtained in terms of (a) flexural strength and (b) fracture toughness for the PM (empty bars) and the GO (dotted bars) specimens. The linear interpolation of the AFt content measured for the PM* (solid lines) and the GO* (dashed lines) specimens is also reported.

Appendix A. – Experimental data related to mechanical and fracture tests

The actual sizes of both the PM and the GO specimens, together with the experimental results, are hereafter reported for all the mechanical tests being performed.

In particular, regarding the flexural testing, the actual sizes of the specimen cross-sections are reported in Tables A.1 and A.2 for the PM and the GO specimens, respectively, by considering all the analysed curing times. Moreover, also the experimental values of the peak load, P_f, and the computed values of the flexural strength, f_{cf}, are listed in such tables. Note that, the nomenclature employed for the specimens is PM_xf_y and GO_xf_y, where x and y stand, respectively, for the curing time and the specimen number.

Table A.1
Flexural tests on the PM specimens: geometric sizes of the cross-section and test results in terms of peak load and strength.

Specimen No.	B [mm]	W [mm]	P_f [kN]	f_{cf} [MPa]
PM-3f-1	40.12	40.00	1.66	4.66
PM-3f-2	40.50	40.00	1.62	4.50
PM-3f-3	40.16	40.00	1.65	4.61
PM-7f-1	41.30	40.00	2.28	6.22
PM-7f-2	40.03	40.00	2.35	6.60
PM-7f-3	40.58	40.00	2.43	6.74
PM-28f-1	41.28	40.00	2.84	7.74
PM-28f-2	41.68	40.00	3.63	9.81
PM-28f-3	40.59	40.00	3.32	9.21
PM-90f-1	39.95	40.00	3.69	10.40
PM-90f-2	39.96	40.00	3.60	10.13
PM-90f-3	39.96	40.00	4.01	11.28
PM-120f-1	41.21	40.00	3.98	10.85
PM-120f-2	40.52	40.00	3.70	10.26
PM-120f-3	41.07	40.00	3.86	10.61

Table A.2
Flexural tests on the GO specimens: geometric sizes of the cross-section and test results in terms of peak load and strength.

Specimen No.	B [mm]	W [mm]	P_f [kN]	f_{cf} [MPa]
GO-3f-1	41.24	40.00	1.78	4.85
GO-3f-2	41.65	40.00	1.75	4.73
GO-3f-3	41.00	40.00	2.02	5.54
GO-7f-1	41.19	40.00	1.84	6.54
GO-7f-2	41.16	40.00	1.99	7.07
GO-7f-3	40.99	40.00	2.16	7.72
GO-28f-1	40.43	40.00	3.59	9.99
GO-28f-2	40.08	40.00	3.37	9.46
GO-28f-3	39.98	40.00	3.60	10.14
GO-90f-1	40.70	40.00	4.13	11.41
GO-90f-2	40.07	40.00	4.33	12.15
GO-90f-3	42.82	40.00	3.99	10.49
GO-120f-1	41.69	40.00	3.75	10.11
GO-120f-2	40.18	40.00	4.45	12.45
GO-120f-3	41.35	40.00	4.14	11.40

As far as the compression testing is concerned, the computed values of the compressive strength, f_c, are reported in Tables A.3 and A.4 for the PM and the GO specimens, respectively, by considering all the analysed curing times. For each specimen type and curing time, six specimens, obtained from the halves of the three broken flexural specimens, are tested. For brevity sake, each f_c value listed in the above tables is the average of the f_c values related to the two halves of the same broken specimen. Note that, the nomenclature employed for such specimens is PM_xc_y and GO_xc_y, being x and y defined as above.

Table A.3

Compression tests on the PM specimens: strength result.

Specimen No.	f_c [MPa]
PM-3c-1	30.78
PM-3c-2	19.74
PM-3c-3	38.04
PM-7c-1	45.73
PM-7c-2	56.03
PM-7c-3	48.11
PM-28c-1	59.91
PM-28c-2	53.71
PM-28c-3	53.62
PM-90c-1	55.27
PM-90c-2	58.66
PM-90c-3	54.22
PM-120c-1	59.68
PM-120c-2	55.27
PM-120c-3	57.45

Table A.4

Compression tests on the GO specimens: strength results.

Specimen No.	f_c [MPa]
GO-3c-1	38.52
GO-3c-2	35.11
GO-3c-3	35.51
GO-7c-1	52.65
GO-7c-2	43.70
GO-7c-3	43.73
GO-28c-1	56.93
GO-28c-2	54.67
GO-28c-3	60.05
GO-90c-1	56.79
GO-90c-2	55.77
GO-90c-3	54.43
GO-120c-1	52.90
GO-120c-2	64.79
GO-120c-3	51.36

Finally, for the fracture testing, the actual sizes of the specimen cross-sections and notch length are reported in Tables A.5 and A.6 for the PM and the GO specimens, respectively, by considering all the analysed curing times. Moreover, also the experimental values of P_{max} and the computed values of both the fracture toughness, $K^S_{(I+II)C}$, and the elastic modulus, E, are listed in such tables. Note that, the nomenclature employed for such specimens is PM_xfr_y and GO_xfr_y, being x and y defined as above.

Table A.5

Fracture toughness tests on the PM specimens: geometric sizes of the cross-section, notch length and test results in terms of peak load, kinking angle, fracture toughness and elastic modulus.

Specimen No.	B [mm]	W [mm]	a_0 [mm]	P_{max} [kN]	α [°]	$K^S_{(I+II)C}$ [MPa·m$^{0.5}$]	E [GPa]
PM-7fr-1	30.18	60.17	20.02	0.52	20.5	0.53	20.22
PM-7fr-2	30.45	61.29	20.29	0.52	23.5	0.52	24.76
PM-7fr-3	30.12	60.82	20.02	0.53	17.5	0.56	23.24
PM-7fr-4	30.51	60.17	19.12	0.54	23.5	0.47	23.10
PM-28fr-1	30.25	60.42	20.16	0.52	16.5	0.51	22.30
PM-28fr-2	29.95	60.25	20.30	0.55	12.0	0.63	24.92
PM-28fr-3	30.37	59.79	18.19	0.54	12.5	0.53	23.16
PM-28fr-4	30.53	60.22	20.06	0.53	21.5	0.56	22.46
PM-90fr-1	29.86	59.74	19.72	0.73	14.0	0.75	22.63
PM-90fr-2	30.65	59.91	20.31	0.76	18.5	0.78	23.09
PM-90fr-3	30.48	59.84	19.04	0.79	20.5	0.80	23.80
PM-90fr-4	30.33	60.10	19.40	0.81	14.5	0.79	21.62

Table A.6

Fracture toughness tests on the GO specimens: geometric sizes of the cross-section, notch length and test results in terms of peak load, kinking angle, fracture toughness and elastic modulus.

Specimen No.	B [mm]	W [mm]	a_0 [mm]	P_{max} [kN]	α [°]	$K^S_{(I+II)C}$ [MPa·m$^{0.5}$]	E [GPa]
GO-7fr-1	30.41	60.98	20.08	0.49	21.0	0.51	21.70
GO-7fr-2	31.07	60.71	20.08	0.51	14.5	0.54	20.90
GO-7fr-3	30.83	60.51	19.87	0.55	10.0	0.64	22.11
GO-7fr-4	30.69	59.39	18.84	0.52	18.5	0.55	20.12
GO-28fr-1	31.37	60.02	19.52	0.66	22.5	0.66	22.09
GO-28fr-2	31.06	60.88	20.01	0.52	11.5	0.61	25.43
GO-28fr-3	30.88	59.80	19.17	0.56	10.5	0.66	23.72
GO-28fr-4	30.67	59.98	19.69	0.59	17.0	0.65	24.05
GO-90fr-1	30.22	60.72	19.29	0.85	17.0	0.87	24.50
GO-90fr-2	31.14	60.10	19.18	0.81	5.5	0.89	26.49
GO-90fr-3	30.59	61.28	20.38	0.85	9.5	0.87	24.66
GO-90fr-4	29.97	59.94	20.06	0.71	13.0	0.81	24.76

References

[1] A. Joshi, P.S. Shivakumar Gouda, I. Sridhar, M.A. Umar Farooq, V.S. Uppin, B. H. Maruthi Prashanth, Influence of matrix modification on interlaminar fracture toughness of glass epoxy laminates using nano and micro fillers, Frattura ed Integrita Strutturale 65 (2023) 59–73.

[2] L.S. Salah, N. Ouslimani, Y. Danlée, F.R. Beltrán, I. Huynen, M. Ulagares de la Orden, Investigation of mechanical recycling effect on electromagnetic properties of polylactic acid (PLA) – nanoclay nanocomposites: towards a valorization of recycled PLA nanocomposites, Compos. Part C Open Access 10 (2023) 100339.

[3] B.P. Shetty, G.J. Naveen, Fractography and tensile studies on the effect of different carbon fillers reinforced hybrid nanocomposites, Frattura ed Integrita Strutturale 66 (2023) 220–232.

[4] D. Zhilyaev, V.D. Fachinotti, F. Zanoni, A. Ortega, G. Goracci, C. Mankel, E.A. B. Koenders, H.M. Jonkers, Early-stage analysis of a novel insulation material based on MPCM-doped cementitious foam: modelling of properties, identification of production process hotspots and exploration of performance trade-offs, Dev. Built Environ. 16 (2023) 100243.

[5] B. Gayretli, R. Shanthar, T.T. Öpöz, C. Abeykoon, Mechanical properties of LDPE and PS polymer matrix composites reinforced with GNP and CF — a critical review, Int. J. Lightweight Mater. Manuf. 7 (2024) 572–596.

[6] M.A. Ghandehari, A.R. Masoodi, Inherent resonance of carbon and graphene-based nanocomposite coupled single-span arch beams, Compos. Part C Open Access 14 (2024) 100458.

[7] T.S. Qureshi, D.K. Panesar, Impact of graphene oxide and highly reduced graphene oxide on cement based composites, Constr. Build. Mater. 206 (2019) 71–83.

[8] T.M.C. dos Reis, V.G. de Castro, L.G. Amurin, G.G. Silva, Graphene oxide dispersion in epoxy resin prepared by direct phase transfer from ethanol: rheology and aging, Compos. Part C Open Access 10 (2023) 100340.

[9] Z. Pan, L. He, L. Qiu, A.H. Korayem, G. Li, J.W. Zhu, F. Collins, D. Li, W.H. Duan, M.C. Wang, Mechanical properties and microstructure of a graphene oxide–cement composite, Cem. Concr. Compos. 58 (2015) 140–147.

[10] M.M. Mokhtar, S.A. Abo-El-Enein, M.Y. Hassaan, M.S. Morsy, M.H. Khalil, Mechanical performance, pore structure and micro-structural characteristics of graphene oxide nano platelets reinforced cement, Constr. Build. Mater. 138 (2017) 333–339.

[11] Y. Wang, J. Yang, D. Ouyang, Effect of graphene oxide on mechanical properties of cement mortar and its strengthening mechanism, Materials. (Basel) 12 (22) (2019) 3753.

[12] Y.-Y. Wu, L. Que, Z. Cui, P. Lambert, Physical Properties Of Concrete Containing Graphene Oxide Nanosheets, Materials. (Basel) 12 (2019) 1707.

[13] S.J. Lee, S.H. Jeong, D.U. Kim, J.P. Won, Effects of graphene oxide on pore structure and mechanical properties of cementitious composites, Compos. Struct. 234 (2020) 111709.

[14] C. Lin, W. Wei, Y.H. Hu, Catalytic behavior of graphene oxide for cement hydration process, J. Phys. Chem. Solids. 89 (2016) 128–133.

[15] S. Lv, Y. Ma, C. Qiu, T. Sun, J. Liu, Q. Zhou, Effect of graphene oxide nanosheets of microstructure and mechanical properties of cement composites, Constr. Build. Mater. 49 (2013) 121–127.

[16] S. Lv, S. Ting, J. Liu, Q. Zhou, Use of graphene oxide nanosheets to regulate the microstructure of hardened cement paste to increase its strength and toughness, Cryst. Eng. Comm. 16 (2014) 8508–8516.

[17] H. Cui, X. Yan, L. Tang, F. Xing, Possible pitfall in sample preparation for SEM analysis - a discussion of the paper "Fabrication of polycarboxylate/graphene oxide nanosheet composites by copolymerization for reinforcing and toughening cement composites, by Lv et al.,, Cem. Concr. Compos. 77 (2017) 81–85.

[18] E. Horszczaruk, E. Mijowska, R.J. Kalenczuk, M. Aleksandrzak, S. Mijowska, Nanocomposite of cement/graphene oxide—impact on hydration kinetics and Young's modulus, Constr. Build. Mater. 78 (2015) 234–242.

[19] M.A. Rafiee, J. Rafiee, Z. Wang, H. Song, Z.-Z. Yu, N. Koratkar, Enhanced mechanical properties of nanocomposites at low graphene content, ACS Nano 3 (2009) 3884–3890.

[20] B. Wang, R. Jiang, Z. Wu, Investigation of the mechanical properties and microstructure of graphene nanoplatelet-cement composite, Nanomaterials 6 (2016) 200.

[21] L. Lu, D. Ouyang, Properties of cement mortar and ultra-high strength concrete incorporating graphene oxide nanosheets, Nanomaterials 7 (2017) 187.

[22] UNI 9156:2015. Sulphates resistant cements – Classification Q6 and composition. 2015.

[23] UNI EN 197-1:2011. Cement – Part 1: composition, specifications and conformity criteria for common cements. 2011.

[24] https://www.buzziunicem.it/tipo-ii (last accessed 12/07/2024).

[25] https://construction.basf.com/global/en.html (last accessed 13/02/2022).

[26] J.C. Pramudita, D. Pontiroli, G. Magnani, M. Gaboardi, M. Riccò, C. Milanese, H.E. A. Brand, N. Sharma, Graphene and selected derivatives as negative electrodes in sodium- and lithium-ion batteries, ChemElectroChem. 2 (4) (2015) 600–610.

[27] M. Gaboardi, R. Tatti, G. Bertoni, G. Magnani, R. Della Pergola, L. Aversa, R. Verucchi, D. Pontiroli, M. Riccò, Platinum carbonyl clusters decomposition on defective graphene surface, Surf. Sci. 691 (2020) 121499.

[28] S. Vantadori, G. Magnani, L. Mantovani, D. Pontiroli, C. Ronchei, D. Scorza, M. Sidoli, A. Zanichelli, M. Riccò, Effect of GO nanosheets on microstructure, mechanical and fracture properties of cement composites, Constr. Build. Mater. 361 (2022) 129368.

[29] UNI EN 1015-3:2007. Methods of test for mortar for masonry - Part 3: determination of consistence of fresh mortar (by flow table). 2007.

[30] A.F. Gualtieri, Accuracy of XRPD QPA using the combined Rietveld–RIR method, J. Appl. Cryst. 33 (2000) 267–278.

[31] A.C. Larson, R.B. Von Dreele, General Structure Analysis System (GSAS). Report LAUR 86-748, Los Alamos National Laboratory, New Mexico, USA, 2004.

[32] B.H. Toby, R.B. Von Dreele, GSAS-II: the genesis of a modern open-source all purpose crystallography software package, J. Appl. Crystallogr. 46 (2013) 544–549.

[33] ASTM C348-14, Standard test method for flexural strength of hydraulic-cement mortars. 2014.

[34] ASTM C349-18, Standard Test Method for Compressive Strength of Hydraulic-Cement Mortars (Using Portions of Prisms Broken in Flexure). 2018.

[35] S.P. Shah, Determination of fracture parameters (KsIC and CTODc) of plain concrete using three-point bend tests, Mater. Struct. Matériaux et Construction 23 (1990) 457–460.

[36] S.P. Shah, A. Carpinteri (Eds.), Fracture Mechanics Test Methods For Concrete –1st Edition, edited by, CRC Press, 1991, pp. 1–10. ISBN 9780367865894,.

[37] S. Vantadori, A. Carpinteri, G. Fortese, C. Ronchei, D. Scorza, Mode I fracture toughness of fibre-reinforced concrete by means of a modified version of the two parameter model, Procedia Struct. Integrity 2 (2016) 2889–2895.

[38] S. Vantadori, F. Berto, G. Fortese, C. Ronchei, D. Scorza, S. Vantadori, Modified two-parameter fracture model for bone, Eng. Fract. Mech. 174 (2017) 44–53.

[39] S. Vantadori, A. Carpinteri, L.-P. Guo, C. Ronchei, A. Zanichelli, Synergy assessment of hybrid reinforcements in concrete, Compos. B: Eng. 147 (2018) 197–206.

[40] D.E. Macphee, E.E. Lachowski, Cement components and their phase relations. In Lea's chemistry of cement and concrete, Pergamon-Elsevier Science Ltd (2003).

[41] A. Madadi, J. Wei, Characterization of calcium silicate hydrate gels with different calcium to silica ratios and polymer modifications, Gels. 8 (2022) 75.

[42] S. Lubej, I. Anžel, P. Jelušič, L. Kosec, A. Ivanič, The effect of delayed ettringite formation on fine grained aerated concrete mechanical properties, Sci. Eng. Compos. Mater. 23 (3) (2016) 325–334.